Shuai He and Ching Tai Ng

Modelling and analysis of nonlinear guided waves interaction at a breathing crack using time-domain spectral finite element method

Smart Materials and Structures, 2017; 26(8):085002-1-085002-15

Modelling and analysis of nonlinear guided waves interaction at a breathing crack using time-domain spectral finite element method

Shuai He and Ching-Tai Ng*

School of Civil, Environmental & Mining Engineering
The University of Adelaide University
Adelaide, SA 5005, Australia

Abstract

This study proposes a time-domain spectral finite element (SFE) model and investigates nonlinear guided wave interaction at a breathing crack. An extended time-domain SFE method based on the Mindlin-Hermann rod and Timoshenko beam theory is proposed to predict the nonlinear guided wave generation at the breathing crack. An SFE crack element is proposed to simulate the mode-conversion effect, in which a bilinear crack mechanism is implemented to take into account the contact nonlinearity at the breathing crack. There is good agreement between the results calculated using the proposed time-domain SFE method and three-dimensional (3D) finite element (FE) simulation. This demonstrates the accuracy of the proposed SFE method in simulating contact nonlinearity at the breathing crack. Parametric studies using the fundamental symmetric (S_0) and anti-symmetric (A_0) modes of guided waves are also carried out to provide physical insights into the higher harmonics generated due to the contact nonlinearity at the breathing crack. The magnitude of the higher harmonics generated as a function of the crack depth is investigated in detail. The results show that the mode-converted higher harmonic guided waves provide valuable information for damage detection.

Keywords: nonlinear guided wave, higher harmonic, spectral finite element, breathing crack, contact nonlinearity

* Corresponding Author: Ching-Tai Ng (Email: alex.ng@adelaide.edu.au)

1. Introduction

Detecting and identifying damage at its early stages is essential for maintaining the safety and serviceability of structures in a wide range of engineering fields, including aerospace, civil and mechanical engineering. Different non-destructive damage detection techniques have been developed for safety inspection. For example, low frequency vibration [1-3], acoustic emission [4] and conventional ultrasonic techniques [5]. Recently, guided waves have been shown to provide a potential cost-effective and reliable safety inspection of structures [6]. Guided waves have been sucessfully applied in plates [7-11], beams [12], and rods [13, 14] for damage detection. Numerous guided wave-based damage detection techniques have been developed, such as time-of-flight approach [15], maximum-likelihood estimation [16], damage imaging [17-21], phase array beamforming [22], model based approach [12, 23] and time-reversal techniques [24].

1.1. Nonlinear guided wave

Most of the aforementioned guided wave-based damage detection techniques assume that the geometry of the damage (e.g. open crack) remains unchanged during the inspection process. The damage detection relies on the linear signal from the damage-wave interaction, i.e. signals at the same frequency as the incident wave. Contact nonlinearity induced by the contact behaviour between crack interfaces was experimentally observed in the literature [25, 26]. Early developments in contact nonlinearity focused on bulk waves; later, nonlinear guided waves attracted significant research attention because of their ability to inspect larger areas compared to bulk waves. When guided wave interacts with a contact-type damage, the compressive pressure of the wave closes the crack, and the tensile pressure opens the crack [6][27]. This phenomenon alters the stiffness of the structure, and produces nonlinear guided wave in the measured signal. In order to improve the accuracy of identification, implementation of the nonlinear guided waves for different types of damages, such as fatigue crack [28], kissing bond [29, 30], delamination [31, 32] and breathing crack [33] have been investigated.

1.2. Numerical methods for predicting nonlinear guided waves

Different methods have been developed to simulate the guided wave propagation in structures [34]. Numerical methods, such as the conventional finite element (FE) method [35, 36], have been used for simulating guided wave propagation in complex structures. However, the FE method is computationally inefficient because the size of the FE elements should be sufficiently smaller than the wavelength of the guided wave to ensure the simulation accuracy. The fast Fourier transform (FFT) based spectral finite element (SFE) method [37-39] is computationally efficient in simulating the guided wave propagation, but it is limited in simulating the cases of finite-length waveguides due to the wrap-around effect [40]. The wavelet spectral finite element (WSFE) overcomes this problem by using the Daubechies scaling functions to approximate the time-dependant variable [41, 42], while it is a semi-analytical method that is impractical for simulating geometrically complicated structures. Other numerical methods also have their limitations in simulating guided wave propagation. For example, the boundary element method [43] would also be significantly inefficient in simulating guided wave propagation when the structure is large. The finite difference (FD) method is unable to simulate guided wave propagation in the waveguide that material property changes with geometry [44]. The finite strip element method [45] is also unsuitable for simulating the geometrically complicated structures.

Recently, the time-domain SFE method has been used to study the guided wave propagation [46], and damage detection [47-50]. The time-domain SFE method [51, 52] has the same flexibility as the FE method in structural discretisation, but it requires fewer elements because it uses high-order shape function to achieve the same level of accuracy as the FE method. The time-domain SFE method applies the Gauss-Lobatto-Legendre (GLL) nodes in the formulation; as a result, a diagonal form of the mass matrix can be obtained. By using the explicit central difference method, therefore, the wave propagation problem can be solved efficiently.

In the literature modelling nonlinear guided waves caused by contact nonlinearity, has been investigated using different methods. These include the FE method [53], FD method [54], local interaction simulation approach (LISA) [55], and the FFT-based SFE method [40, 56]. However, an efficient time-domain SFE method has not yet been developed for this purpose. In this study, the time-domain SFE method is extended to simulate the nonlinear guided wave generated at cracks, where the nonlinear crack-wave interaction is simulated by contact mechanism. This study also

provides physical insights into the generation of nonlinear guided waves (e.g. higher harmonics) resulting from the contact nonlinearity. This helps to further advance the use of the nonlinear guided waves in damage detection.

In practical situations, the mode-conversion phenomenon occurs when guided waves interact with an asymmetric discontinuity. Specifically, the mode-conversion effect of guided waves is a phenomenon by which a purely axial input gives rise to flexural response and vice versa. The fundamental anti-symmetric mode (A_0) guided wave can be generated when the fundamental symmetric mode (S_0) guided wave interacts with an asymmetric discontinuity and vice versa. In the literature, the study of the mode-conversion effect has been limited to linear guided waves. For example, the mode-converted linear guided wave signal has been employed to detect delaminations in composite laminates [23], and cracks in aluminium beams [57]. In contrast, there are a very limited number of studies focused on the mode conversion of nonlinear guided waves. In this study the mode-conversion effect of the nonlinear guided waves is investigated using the proposed time-domain SFE method and the SFE crack element. The mode-conversion effect of A_0 guided waves converted to S_0 nonlinear guided waves, and vice versa, is studied in detail.

The paper is organised as follows. The time-domain SFE method is first presented in Section 2, where a bilinear crack model is embedded in the SFE crack element to simulate contact nonlinearity at the breathing crack. In Section 3, the proposed time-domain SFE method is validated using the conventional 3D FE method. This section compares SFE and 3D FE simulated signals with generated higher harmonics that result from the contact nonlinearity at the breathing crack. The detailed comparison examines both time and frequency of the signals. Section 4 provides an observation of the generated nonlinear guided waves and investigates the mode-conversion effect of the nonlinear guided waves at the crack. Section 5 presents a series of parametric studies that investigate the characteristics of the generated, higher harmonic guided waves, in which the magnitude of the generated higher harmonics as a function of the crack depth is studied. Finally, the conclusions are drawn in Section 6.

2. Time-domain spectral finite element method

2.1. Spectral finite element (SFE) formulation

The SFE method employs a similar time-domain dynamic equilibrium as the conventional FE method, which has the following form [52, 58, 59]

$$\mathbf{M}\ddot{\mathbf{U}} + \mathbf{C}\dot{\mathbf{U}} + \mathbf{K}\mathbf{U} = \mathbf{F}\left(t\right) \tag{1}$$

where $\mathbf{U}$, $\dot{\mathbf{U}}$ and $\ddot{\mathbf{U}}$ are the global vectors corresponding to nodal displacement, velocity and acceleration, respectively. $\mathbf{M}$, $\mathbf{C}$, $\mathbf{K}$ and $\mathbf{F}\left(t\right)$ denote the global mass matrix, global damping matrix, global stiffness matrix and global force vector at time t, respectively. Specifically, the damping matrix $\mathbf{C}$ is proportional to the global mass matrix as $\mathbf{C} = \eta\mathbf{M}$, where η is the damping coefficient. In addition, the global matrixes, $\mathbf{M}$ and $\mathbf{K}$ and the global force vector $\mathbf{F}\left(t\right)$, are assembled from their corresponding elemental terms $\mathbf{M}^e$, $\mathbf{K}^e$ and $\mathbf{F}^e$, which can be expressed as

$$\mathbf{M}^e \approx \sum_{i=1}^{n} w_i \mathbf{S}_e\left(\xi_i\right)^T \boldsymbol{\rho}_e \mathbf{S}_e\left(\xi_i\right)\left|J\left(\xi_i\right)\right| \tag{2}$$

$$\mathbf{K}^e \approx \sum_{i=1}^{n} w_i \mathbf{B}_e\left(\xi_i\right)^T \mathbf{E}_e \mathbf{B}_e\left(\xi_i\right)\left|J\left(\xi_i\right)\right| \tag{3}$$

$$\mathbf{F}^e \approx \sum_{i=1}^{n} w_i \mathbf{S}_e\left(\xi_i\right)^T \mathbf{f}_e\left(\xi_i\right)\left|J\left(\xi_i\right)\right| \tag{4}$$

where n is the node number in the element, $\mathbf{f}_e\left(\xi_i\right)$ is the external force and ξ_i is the local coordinate of the node i in the element, respectively. $J = \partial x/\partial\xi$ is the Jacobian function mapping the local coordinate ξ to the global coordinate x. Distinct from the conventional FE method, the nodes in the SFE are called GLL nodes [57]. The local coordinate ξ of each node in the SFE can be obtained as the roots of the following equation

$$\left(1-\xi_i^2\right)L'_{n-1}\left(\xi_i\right) = 0,\ i \in 1,\ldots,n \tag{5}$$

where L_{n-1} is the Legendre polynomial in (n-1)-th order and the symbol "$'$" denotes the differential operation. w_i is the weighting function of node i and it can be calculated as

$$w_i = \frac{2}{n\left(n-1\right)\left[L_{n-1}\left(\xi_i\right)\right]^2} \tag{6}$$

$\mathbf{S}_e$ is the shape function matrix defined as

$$\mathbf{S}_e = \mathbf{S} \otimes \mathbf{I} \tag{7}$$

where $\mathbf{S} = [\ S_1(\ )\ \ ...\ \ S_n(\ )\ ]^T$, ' $\otimes$ ' is the Kronecker product and $\mathbf{I}$ is a square identity matrix having the same size as the number of nodal degree-of-freedoms (DoFs), respectively. $S_i(\ )$ is the spectral shape function value for node *i* defined as

$$S_i(\xi) = \prod_{m=1, m\neq i}^{n} \frac{\xi - \xi_m}{\xi_i - \xi_m} \tag{8}$$

Due to the Kronecker property of the shape function value, the mass matrix achieves a diagonal form. It can be solved efficiently by the explicit central difference method. The number of elements needed to capture guided wave propagation accurately can be significantly reduced by using the GLL nodes, thus improving the computational efficiency of the SFE method.

In this study, Equation (1) is governed by the Mindlin-Herrmann rod theory and Timoshenko beam theory. The independent lateral contraction $\psi(x)$ is introduced to account for the Poisson effect. The first order shear deformation is considered by employing an independent rotation $\varphi(x)$. Based on the Mindlin-Herrmann rod theory and Timoshenko beam theory, the displacement field of the beam is

$$\begin{aligned} \bar{u}(x, y) &\approx u(x) - \varphi(x)\, y \\ \bar{v}(x, y) &\approx v(x) + \psi(x)\, y \end{aligned} \tag{9}$$

where $u(x)$ and $v(x)$ are the longitudinal and transverse displacements at *x* axis, respectively. The strain field $\boldsymbol{\varepsilon}$ at the *x* axis of the beam can be obtained in a matrix form as

$$\boldsymbol{\varepsilon} = \mathbf{B}_e \mathbf{q} \tag{10}$$

where $\mathbf{q} = \begin{bmatrix} u & v \end{bmatrix}^T$ is the displacement field vector and $\mathbf{B}_e$ is the constitutive relation between strain and displacement. It is defined as

$$\mathbf{B}_e = \begin{bmatrix} \frac{\partial}{\partial x} & 0 & 0 & 0 \\ 0 & 1 & 0 & 0 \\ 0 & \frac{\partial}{\partial x} & 0 & 0 \\ 0 & 0 & \frac{\partial}{\partial x} & -1 \\ 0 & 0 & 0 & \frac{\partial}{\partial x} \end{bmatrix} \mathbf{S}_e \tag{11}$$

According to the Mindlin-Herrmann rod and Timoshenko beam theories the mass density matrix $\boldsymbol{\rho}_e$ and the stress-strain matrix $\mathbf{E}_e$ in Equations (2) and (3) have the following form

$$\boldsymbol{\rho}_e = \begin{bmatrix} \rho A & 0 & 0 & 0 \\ 0 & K_2^M \rho I & 0 & 0 \\ 0 & 0 & \rho A & 0 \\ 0 & 0 & 0 & K_2^T \rho I \end{bmatrix} \tag{12}$$

and

$$\mathbf{E}_e = \begin{bmatrix} \frac{EA}{1-\nu^2} & \frac{\nu EA}{1-\nu^2} & 0 & 0 & 0 \\ \frac{\nu EA}{1-\nu^2} & \frac{EA}{1-\nu^2} & 0 & 0 & 0 \\ 0 & 0 & K_1^M GI & 0 & 0 \\ 0 & 0 & 0 & K_1^T GA & 0 \\ 0 & 0 & 0 & 0 & EI \end{bmatrix} \tag{13}$$

where ρ, A and I denotes the density of the material, the cross-section area of the beam, and the moment of inertia, respectively. E, G and are the Young's modules, shear modules and Poisson's ratio, respectively. K_1^M, K_2^M, K_1^T and K_2^T are adjustable parameters that calibrate the accuracy guided wave propagation simulation. In this paper, the value K_1^M = 1.1, K_2^M = 3.1 and K_1^T = 0.922 are determined from the experimental data in our previous study [57], by which the SFE simulation has the best fitting to the experimental data. K_2^T is set as $12K_1^T/\pi^2$ to match the cut-off frequency of guided wave modes.

2.2. Open crack model

An SFE crack element was developed to model an open crack [57]. The mode-conversion effect is simulated by coupling the longitudinal, transverse and rotational DoFs in the crack element. The crack element has two nodes and has a very small length, i.e. $l = 0.1$ mm. As shown in Figure 1, in the aluminium beam with thickness b and height h, the crack is located at l_c in the SFE crack element. The cross-section of the crack is rectangular, where the width and depth are b and d_c, respectively. In the crack element, lateral contraction due to the longitudinal guided wave propagation is not considered because the length of the element is very small. Hence, the nodes in the crack element consider only the longitudinal, transverse and rotational DoFs. The stiffness matrix $\mathbf{K}_e^c$ is developed for the crack element using a similar approach, [60] but it has been modified because of the rectangular cross-section of the beam in this study.

[Figure 1. Schematic diagram of the two-node crack element for simulating an opened crack. (a) Discretization of a cracked beam; (b) SFE crack element]

In this paper, the crack element stiffness matrix $\mathbf{K}_e^c$ has the form

$$\mathbf{K}_e^c = \mathbf{P}\mathbf{G}_c^{-1}\mathbf{P}^T \tag{14}$$

where $\mathbf{P}$ is the spatial transformation matrix as a function of the crack element length l

$$\mathbf{P}^T = \begin{bmatrix} 1 & 0 & 0 & -1 & 0 & 0 \\ 0 & 1 & 0 & 0 & -1 & l \\ 0 & 0 & 1 & 0 & 0 & -1 \end{bmatrix} \tag{15}$$

$\mathbf{G}$ is the flexibility matrix given as follows

$$\mathbf{G}_c = \begin{pmatrix} g_{11}^c & g_{12}^c & g_{13}^c \\ g_{21}^c & g_{22}^c & g_{23}^c \\ g_{31}^c & g_{32}^c & g_{33}^c \end{pmatrix} \tag{16}$$

with

$$g_{11} = \frac{l}{EA} + I_{g1},\ g_{22} = \left(\frac{\kappa l}{GA} + \frac{l^3}{3EA}\right) + \left(I_{g3} + l_c^2 I_{g4}\right),\ g_{33} = \frac{l}{EI} + I_{g4},$$

$$g_{12} = g_{21} = l_c I_{g2},\ g_{13} = g_{31} = -I_{g2},\ g_{23} = g_{32} = -\frac{l^2}{2EI} - l_c I_{g4} \tag{17}$$

where $\kappa = 10(1+\nu)/(12+11\nu)$ is the shear coefficient for the rectangular beam cross section. I_{g1}, I_{g2}, I_{g3} and I_{g4} are functions of the crack depth, defined as

$$I_{g1} = \frac{2\pi}{Eb}\int_0^{\alpha} \alpha F_1^2 d\alpha$$

$$I_{g2} = \frac{12\pi}{Ebh}\int_0^{\alpha} \alpha F_1 F_2 d\alpha$$

$$I_{g3} = \frac{2\kappa\pi}{Eb}\int_0^{\alpha} \alpha F_{II}{}^2 d\alpha$$

$$I_{g4} = \frac{72\pi}{Ebh^2}\int_0^{\alpha} \alpha F_2{}^2 d\alpha \tag{18}$$

where $\alpha = d_c / h$. F_1, F_2 and F_{II} are the empirical boundary calibration factors accounted for tension, bending and shear for the surface crack, for which formulations are given as Tada, Paris, Irwin and Tada [61]

$$F_1(\alpha) = \sqrt{\frac{2}{\pi\alpha}\tan\left(\frac{\pi\alpha}{2}\right)}\frac{0.752 + 2.02\alpha + 0.37\left[1-\sin\left(\frac{\pi\alpha}{2}\right)\right]^3}{\cos\left(\frac{\pi\alpha}{2}\right)} \tag{19}$$

$$F_2(\alpha) = \sqrt{\frac{2}{\pi\alpha}\tan\left(\frac{\pi\alpha}{2}\right)}\frac{0.923 + 0.199\left[1-\sin\left(\frac{\pi\alpha}{2}\right)\right]^4}{\cos\left(\frac{\pi\alpha}{2}\right)} \tag{20}$$

$$F_{II}(\alpha) = \frac{1.122 - 0.561\alpha + 0.085\alpha^2 + 0.18\alpha^3}{\sqrt{1-\alpha}} \tag{21}$$

According to Tada, Paris, Irwin and Tada [61], the factors F_1, F_2 and F_{II} produce less than 0.5% errors for a crack with any depth d_c. It should be noted that if the crack is closed, the crack element is treated as an intact SFE beam element, and its stiffness matrix $\mathbf{K}_e^c$ in Equation (14) becomes

$$\mathbf{K}_e^c = \mathbf{P}\mathbf{G}_e^{-1}\mathbf{P}^T \tag{22}$$

where $\mathbf{G}_e$ is the flexibility matrix for the closed crack element as follows

$$\mathbf{G}_e = \begin{pmatrix} g_{11}^e & g_{12}^e & g_{13}^e \\ g_{21}^e & g_{22}^e & g_{23}^e \\ g_{31}^e & g_{32}^e & g_{33}^e \end{pmatrix} \tag{23}$$

with

$$g_{11}^e = \frac{l}{EA},\ g_{22}^e = \left(\frac{\kappa l}{GA} + \frac{l^3}{3EA}\right),\ g_{33}^e = \frac{l}{EI},$$

$$g_{12}^e = g_{21}^e = g_{13}^e = g_{31}^e = 0,\ g_{23}^e = g_{32}^e = -\frac{l^2}{2EI} \tag{24}$$

2.3. Crack-breathing mechanism

When the incident guided wave interacts with the crack, the contact nonlinearity occurs due to the crack-breathing phenomenon. There are numerous methods for simulating the contact nonlinearity of guided waves, but the bilinear crack model is one of the most commonly used approaches [33, 62]. In this paper, a bilinear crack mechanism is proposed for taking into account the contact nonlinearity effect, and it is incorporated in the SFE crack model. Specifically, when the out-of-plane excitation is applied, the nodal rotations φ_1 and φ_2 of the two-node crack element are examined at each step. On the other hand, when the in-plane excitation is applied, the nodal longitudinal displacements u_1 and u_2 are examined. These are shown in the following equations

Out-of-plane excitation:

Crack open:

$$\varphi_1 - \varphi_2 > 0 \tag{25}$$

Crack closed:

$$\varphi_1 - \varphi_2 <= 0 \tag{26}$$

In-plane excitation:

Crack open:

$$u_1 - u_2 < 0 \tag{27}$$

Crack closed:

$$u_1 - u_2 >= 0 \tag{28}$$

These mechanisms are indicated in Figure 2. If the crack is open, the proposed SFE open crack element is used. When the crack is closed, the SFE crack element is treated as an intact SFE beam element. By replacing the stiffness matrix of the crack element, the contact nonlinearity effect can be simulated.

[Figure 2. Degrees-of-freedom at the crack element when the crack is (a) opened and (b) closed]

3. Validation using three-dimensional finite element simulation

In order to verify the accuracy of the proposed SFE method, the results of a beam modelled using the time-domain SFE method are compared with the results calculated using the conventional explicit three-dimensional (3D) FE method. The verification is conducted in two different situations: 1) exciting S_0 and 2) A_0 incident guided waves. It is assumed that the beam is made of aluminium and the material properties are shown in Table 1. The width and height of the beam are b = 12 mm and h = 6 mm, respectively. A schematic diagram of the beam is shown in Figure 3. The beam length, crack location and number of SFE elements used for these two different situations are shown in Table 1.

[Figure 3. Schematic diagram of a beam with a surface breathing crack]

[Table 1. Summary of the time-domain SFE models used in the validation]

The excitation signal is a f_0 = 25 kHz, narrow-band, 5-cycle sinusoidal tone burst modulated by a Hanning window [63]. Using this frequency is to ensure that only the fundamental guided wave modes (e.g. A_0 and S_0) are generated in both the fundamental and higher harmonic frequencies. The excitation signal was induced by applying a boundary displacement in the in-plane and out-of-plane directions of the SFE node at the beam's left end (x = 0 m) to generate the S_0 and A_0 incident guided waves, respectively. According to the dispersion relation predicted by the SFE model in Figure 4, only the S_0 and A_0 incident guided waves are generated. The nodal velocity is calculated at x = 0 m, which is the same location as the excitation. The calculated velocity is normalised by the maximum amplitude of incident wave velocity. The

calculated duration is long enough to cover the incident guided wave propagates from the excitation to the right beam end, and back to the measurement location. The damping coefficient η is chosen to be 550 s^{-1} [57]. Eight GLL nodes in each SFE beam element are used in the model. The time step for solving the dynamic Equation (1) is 0.25×10^{-7} s.

[Figure 4. Dispersion relations for an aluminum beam predicted by the SFE model (a) Phase velocity; (b) Group velocity]

For the 3D FE model, commercial FE software, ABAQUS v6.12-1, is used to simulate the guided waves in the beam. Eight-node 3D incompatible modes solid brick elements (C3D8I) are employed to model the cracked beam and the second-order accuracy is enabled in the modelling. The S_0 and A_0 incident guided wave are generated by applying the excitation signal as a surface traction in in-plane and out-of-plane direction, respectively, at the vertical surface of the beam's left end. The mesh size of the FE element is 0.4mm×0.4mm×0.4mm to ensure the stability of the simulations. The dynamic problem is solved by explicit solver, ABAQUS/Explicit. The time step in the FE simulation is automatically controlled by ABAQUS/Explicit. The breathing crack is modelled by duplicating the nodes at the crack surfaces and the 'frictionless hard contact' property is assigned to the crack surfaces, which allows the simulation of the contact nonlinearity when guided waves interact with the crack.

The comparison of the SFE and explicit 3D FE simulated results are shown in Figures 5 to 6, where S_0 guided wave is used as the incident wave first. Figures 5a and 5b show the in-plane and out-of-plane velocity in time-domain. The signals are normalized such that the maximum amplitude of S_0 incident wave package is unity. For the incident S_0 guided wave, there is good agreement between signals calculated by the time-domain SFE method and the explicit 3D FE method in the arrival time, amplitude of in-plane velocity (S_0 guided wave), the mode-converted out-of-plane velocity (mode-converted A_0 guided wave) and the signal distortion due to the contact nonlinearity at the crack. The corresponding normalized spectral amplitudes of the Fourier-transformed time-domain velocity are shown in Figures 6a and 6b, respectively. There is good agreement between the results of the Fourier-transformed velocity responses calculated using SFE and explicit 3D FE methods at the excitation frequency and higher harmonic frequencies. Comparing Figures 6a and 6b, it indicates that the energy of higher

harmonics generated due to the interaction of the S_0 incident guided wave with the crack is mainly concentrated in the mode-converted A_0 nonlinear guided waves.

[Figure 5. Time-domain (a) in-plane and (b) mode-converted out-of-plane velocity at x = 0 m for incident S_0 guided wave from time-domain SFE and 3D FE simulation]

[Figure 6. Fourier-transformed (a) in-plane and (b) mode-converted out-of-plane velocity at x = 0 m for incident S_0 guided wave from time-domain SFE and 3D FE simulation]

Figures 7 and 8 show the time domain velocity response and the corresponding spectral amplitude when the incident wave is the A_0 guided wave. Similar to the incident S_0 guided wave, there is good agreement between the time-domain SFE and explicit 3D FE simulations. However, there is a slight difference in the out-of-plane velocity responses as shown in Figure 8a. The very small discrepancy shown in Figure 8a is mainly due to the one-dimensional (1D) assumption in the time-domain SFE but the FE simulations are in 3D, and the limitation of the first order beam theory used in the SFE beam formulation. Comparing Figure 8 with Figure 6, it shows that the energy of the higher harmonics in the mode-converted S_0 guided wave, which is induced by the crack-wave interaction using the A_0 incident guided wave, is much less than that in the mode-converted A_0 guided wave when the incident wave is the S_0 guided wave.

The results in Figures 5 – 8 show reasonably good agreement, including the generated higher harmonics due to contact nonlinearity at the breathing crack. Therefore, the proposed time-domain SFE model is able to simulate the nonlinear guided wave induced due to contact nonlinearity and the mode-conversion effect accurately.

[Figure 7. Time-domain (a) out-of-plane and (b) mode-converted in-plane velocity at x = 0 m for incident A_0 guided wave from time-domain SFE and 3D FE simulation]

[Figure 8. Fourier-transformed (a) out-of-plane and (b) mode-converted in-plane velocity at x = 0 m for incident A_0 guided wave from time-domain SFE and 3D FE simulation]

4. Higher harmonics generation due to contact nonlinearity at breathing crack

The generation of higher harmonics is studied in this section using the time-domain SFE method. An aluminium beam is modelled, which has the same cross-section and material properties as the aluminium beam used in Section 3. Two scenarios, S_0 and A_0 incident guided waves, are considered separately. The length L of the beam, the crack locations L_c and the measured locations are different in these two scenarios, and they are summarised in Table 2. For each scenario, we investigate four different cases considering different effects of the contact nonlinearity and mode-conversion. The excitation signal is an f_0 = 25 kHz, narrow-band, 5-cycle sinusoidal tone burst modulated by a Hanning window, and it is applied as a force at the left end of the beam.

[Table 2. Summary of case studies for higher harmonic generation due to contact nonlinearity at the breathing crack]

4.1. Incident S_0 guided wave

The incident S_0 guided wave is excited by applying the in-plane external force to the left end of the beam. The in-plane response is investigated in subsection 4.1.1 and the mode-converted out-of-plane response is studied in subsection 4.1.2.

4.1.1. In-plane response

In this subsection the excitation is applied in the in-plane direction to generate the incident S_0 guided wave. Four different cases, S1, S2, S3 and S4, as shown in Table 2, are considered in studying the generation of higher harmonics due to the S_0 guided wave's interaction with the breathing crack. Case S1 does not simulate the contact nonlinearity and mode-conversion effect at the breathing crack. The mode conversion effect is not considered by removing the coupling terms e.g., g_{12} and g_{13} in Equation (17) in the SFE crack element. Case S2 only simulates the contact nonlinearity effect by utilising the bilinear crack model. Case S3 simulates both contact nonlinearity and the

mode-conversion effect. Case S4 considers only the mode conversion effect without the contact nonlinearity.

The S_0 guided wave propagation is studied first. Figure 9 shows the in-plane velocity time histories at different locations along the beam for Case S3, in which both contact nonlinearity and the mode-conversion effect are considered. It should be noted that Figure 9 only shows the in-plane velocity, where only the linear and second harmonic S_0 guided waves are visualized in the time histories. Figure 9 shows that when the incident S_0 guided wave (indicated by the solid red lines) encounters the breathing crack, it separates into two wave packages: transmitted waves and reflected waves. The second harmonic guided wave, indicated by the blue dashed line at the frequency $2f_0$, which occurred induced due to the contact nonlinearity effect, is not observed from the in-plane velocity in the time-domain. This is because the linear (f_0) and the second harmonic ($2f_0$) S_0 guided waves have very similar group velocities as shown in Figure 4. As a result, they mix together during the wave propagation.

[Figure 9. In-plane velocity of S_0 guided wave time histories at different locations along the beam for Case S3]

In order to investigate the higher harmonics induced by the contact nonlinearity at the breathing crack, the energy density spectrum for each damage case is calculated using the Gabor wavelet transform [17, 64]. The baseline subtraction technique [17] is used to extract the scattered wave signals from the breathing crack, i.e. the linear scattered S_0 guided waves and the nonlinear S_0 guided waves. The S_0 guided wave signal is measured at x = 5 m and the baseline data is obtained from an intact SFE beam. The extracted wave signals for Cases S1-S4 are shown in Figure 10. Figure 10 shows that the time-domain response is plotted from 900 to 2400 μs because there is no extracted guided wave signal before 900 μs, where each of the wave packages can be identified using Figure 9. Note that resulting from the similar group velocity of S_0 guided wave for each harmonic shown Figure 4, each guided wave package contains both the fundamental and second harmonics if considering the contact nonlinearity effect.

[Figure 10. Extracted time domain in-plane velocity signal from 900 - 2400 μs at x = 5 m for (a) Cases S1, (b) S2, (c) S3 and (d) S4]

Figures 10a considers no contact nonlinearity and mode-conversion effect. Each guided wave package has the largest amplitude compared with other cases. Comparing Figures 10b and 10d, it is shown that when the mode conversion effect is considered alone, the amplitude of each guided wave package decreases less than that only considering the contact nonlinearity. While in Figure 10(c), where both the contact nonlinearity and mode conversion effect are considered, the amplitude of each guided wave package becomes the smallest compared with other cases.

[Figure 11. Energy density spectrum of the in-plane velocity signal from 900 - 2400 μs at measurement location x = 5 m for (a) Cases S1, (b) S2, (c) S3 and (d) S4]

The corresponding energy density spectra are shown in Figure 11. It should be noted that the magnitude of the energy density spectrum is normalized to 1 for the first wave package of the extracted signal of the transmitted guided wave. Figure 11a shows the energy density spectrum of Case S1, in which the contact nonlinearity and mode-conversion effect are not considered. Hence, the energy of the extracted wave signals concentrates at the excitation frequency (f_0 = 25 kHz) and no higher harmonics are generated.

Case S2 considered the contact nonlinearity effect. As shown in Figure 11b, the second harmonic at the frequency $2f_0$ = 50 kHz is observed in the energy density spectrum. This shows that the nonlinear S_0 guided wave is generated due to the contact nonlinearity effect.

Case S3 in Figure 11c considers both the contact nonlinearity and mode-conversion effect. The energy at the second harmonic frequency ($2f_0$ = 50 kHz) is weaker compared to that in Case S2. This indicates that part of the energy of the S_0 nonlinear guided wave is converted to the A_0 nonlinear guided wave due to the mode-conversion effect. However, the linear components of the energy spectrum are similar to Figure 11b. This is because the spectral amplitude of the higher harmonic is very small compared to the linear component, and the energy spectrum has linear relation to the square of the spectral amplitude, this results a small change to the linear component than the higher harmonic in the energy spectrum in Figure 11c.

Case S4, as shown in Figure 11d, considers only the mode conversion effect without the contact nonlinearity. It is shown that the energy spectrum at the frequency f_0

of each guided wave package is slightly less than that in Figure 11a. Also, no higher harmonics are generated. The results of the out-of-plane velocity, i.e. the A_0 linear and nonlinear guided waves are presented in the next sub-section.

4.1.2. Mode-converted out-of-plane response

The mode-converted out-of-plane velocity at different locations along the SFE beam for Case S3 is shown in Figure 12, in which both the contact nonlinearity and the mode-conversion effect are considered in the simulation. As shown in Figure 12, the mode-converted S_0-A_0 guided waves (i.e., A_0 guided waves converted from S_0 incident-guided waves) are generated when the S_0 incident-guided wave interacts with the crack. Due to the contact nonlinearity effect, higher harmonics with frequencies at f_0, $2f_0$, $3f_0$ and $4f_0$, are generated in the out-of-plane velocity. These mode-converted A_0 higher harmonic guided waves propagate at different velocities, in which the first harmonic has the lowest group velocity, while the fourth harmonic has the highest group velocity. As shown in Figure 12, the S_0-A_0 guided waves at frequency f_0, $2f_0$, $3f_0$ and $4f_0$ are denoted by a solid red line, a dash-dot blue line, a dashed blue line and a dotted red line, respectively. This shows that the mode-conversion effect induces not only the linear mode-converted waves but also the nonlinear mode-converted guided waves due to the contact nonlinearity at the asymmetrical breathing crack.

[Figure 12. Out-of-plane velocity of mode-converted S_0-A_0 guided wave time histories at different locations along the beam for Case S3 (the normalised amplitude is amplified by a factor of 3)]

The energy density spectrum of the mode-converted A_0 guided wave measured at x = 5 m is shown in Figure 13. There are four wave packages as shown in Figure 13a, and the corresponding energy density spectrum of the first (f_0) and the second ($2f_0$) harmonics are shown in Figure 13b. The energy of the third ($3f_0$) and the fourth ($4f_0$) harmonics are too small to be shown after the normalisation. Hence, the energy density spectrum only shows the first and the second harmonics. The results in Figure 13 successfully demonstrate mode-converted A_0 higher harmonic guided waves generated as a result of the contact nonlinearity effect.

[Figure 13. Time history and energy density spectrum of the out-of-plane velocity signal from 900 - 2400 μs at measurement location x = 5 m for Cases S3]

4.2. Incident A_0 guided wave

The incident A_0 guided wave is excited by applying the out-of-plane external force to the left end of the beam. The out-of-plane response is investigated in subsection 4.2.1 and the mode-converted in-plane response is studied in subsection 4.2.2.

4.2.1. Out-of-plane response

This subsection investigates the nonlinear guided wave generated due to the interaction of the A_0 guided wave with the breathing crack. The calculated time histories at different locations along the beam for Case A3, in which both contact nonlinearity and mode-conversion effect are considered, are shown in Figure 14. When an f_0 = 25 kHz incident A_0 guided wave encounters the crack, a linear reflected wave and a linear transmitted wave (f_0 = 25 kHz) occur, which are indicated by solid red lines in Figure 14. Due to the contact nonlinearity, the higher harmonic A_0 guided waves ($2f_0$ = 50 kHz) are also generated. They propagate in forward and backward directions from the crack, and they are indicated by dashed blue lines. Because of the dispersive nature of the low frequency A_0 guided waves, the A_0 guided waves at f_0 and $2f_0$ frequency propagate at different group velocities. Since the crack is asymmetric, the S_0 guided wave is also converted from the incident A_0 guided wave. It is not shown in the Figure 14, however, because only the out-of-plane velocity is shown. When the mode-converted S_0 guided wave interacts with the asymmetrical crack, it induces the mode-converted A_0 guided wave, i.e. A_0-S_0-A_0 guided waves. The A_0-S_0-A_0 guided waves at f_0 and $2f_0$ frequency are indicated by the dotted red line and dashed-dotted blue line, respectively.

[Figure 14. Out-of-plane velocity of A_0 guided wave and mode-converted A_0-S_0-A_0 guided wave time histories at different locations along the beam for Case A3]

[Figure 15. Extracted time-domain out-of-plane velocity signal from 500 - 2100 μs at x = 1.65 m for (a) Cases A1, (b) A2, (c) A3 and (d) A4]

Figures 15a, 15b, 15c and 15d show the out-of-plane velocity time history at measurement location x = 1.65 m for Cases A1, A2, A3 and A4, respectively. The scattered wave is extracted using a baseline subtraction technique [17]. Figure 16 shows the corresponding energy density spectrum of the time histories depicted in Figure 15. The energy density spectrum is used to investigate the influence of the contact nonlinearity and mode-conversion effect. The magnitude of the energy density spectrum is normalised to 1 for the extracted, transmitted guided wave package, i.e., GW-1 shown in Figure 15a. Figure 16 only shows the magnitude in the range from 0 to 0.2 for the normalised energy density spectrum.

For Case A1 no contact nonlinearity or mode-conversion effects are considered. There are only two guided wave packages: the forward scattered wave passing through the crack, and its reflection from the right beam end, which are labelled as GW-1 and GW-2 in Figure 15a, respectively. The corresponding energy density spectrum shown in Figure 16a indicates that there is no higher harmonic. In contrast, the results from Case A2, in which the contact nonlinearity effect is considered, indicate the existence of higher harmonic guided waves in Figure 16b. In that figure, guided wave packages, GW-1 and GW-2, contain signals at two different frequencies: the excitation frequency f_0 and the second harmonic frequency $2f_0$, respectively. For GW-3, it only has signal at the second harmonic $2f_0$. Case A3 considers both contact nonlinearity and the mode-conversion effect. In addition to GW-1, GW-2 and GW-3, a guided wave package GW-4 is observed in Figure 16c. GW-4 contains the mode-converted A_0-S_0-A_0 guided waves at the excitation frequency f_0 and at the second harmonic frequency $2f_0$. They are induced by the contact nonlinearity and mode-conversion effect at the asymmetric crack. In Case A4, the contact nonlinearity is removed and only the mode-conversion effect is considered in the simulation. The guided wave package GW-3 caused by contact nonlinearity is disappeared in Figure 15d. The guided wave packages GW-1 and GW-2 and GW-4 only contain the linear component as shown in the energy spectrum in Figure 16d.

[Figure 16. Energy density spectrum of the out-of-plane velocity signal from 500 - 2100 μs at measurement location x = 1.65 m for (a) Cases A1, (b) A2, (c) A3 and (d) A4]

4.2.2. Mode-converted in-plane response

Figure 17 shows the propagation of the mode-converted A_0-S_0 guided waves. The amplitude is increased by a coefficient of 5. The mode-converted A_0-S_0 guided wave is generated at the moment when the incident A_0 guided wave encountered the asymmetrical crack. Due to the contact nonlinearity effect, both mode-converted A_0-S_0 guided waves at f_0 and $2f_0$ are generated. The solid red line and dash-dot blue line indicate the f_0 and $2f_0$ mode-converted A_0-S_0 guided waves, respectively. As they have similar group velocities, they are mixed together in the time-domain. The reflected, mode-converted A_0-S_0 guided waves are then reflected from the beam's left end. These waves propagate forwards and encounter the breathing crack. They then generate the mode-converted A_0-S_0-A_0 guided waves observed in Figure 14 (dotted red line for the linear A_0-S_0-A_0 guided waves and dashed-dotted blue line for the second harmonic A_0-S_0-A_0 guided waves).

[Figure 17. In-plane velocity of mode-converted A_0-S_0 guided wave time histories at different locations along the beam for Case A3 (the normalised amplitude is amplified by a factor of 5)]

The velocity time history and the corresponding energy density spectrum of the mode-converted A_0-S_0 guided waves at the measurement location x = 1.65 m for Case A3 are shown in Figures 18a and 18b, respectively. The mode-converted A_0-S_0 guided waves at frequencies f_0 and $2f_0$ are mixed together in the time-domain as they have similar group velocities. This is consistent with the energy density spectrum as the energy for each guided wave package in Figure 18b is centred at both the f_0 and $2f_0$ frequencies. In addition, by comparing the energy density spectrum in Figure 18b with that in Figure 16c, we can see that the mode-converted A_0-S_0 higher harmonic guided waves are easier to observe as they have larger magnitudes.

[Figure 18. Energy density spectrum of the in-plane velocity signal from 500 - 2100 μs at measurement location x = 1.65 m for Cases A3]

5. Parametric studies

This section investigates the characteristics of incident guided waves and mode-converted higher harmonic guided waves for different crack depths. In each study, the excitation force was an f_0 = 25 kHz, narrow-band, 5-cycle sinusoidal tone burst modulated by a Hanning window. The excitation is applied in both in-plane and out-of-plane directions to generate the S_0 and A_0 guided waves, respectively. The length of the aluminium beam is 1 m and the crack location is x = 0.5 m. The baseline subtraction technique [17] is used in the study to extract the scattered wave signals from the breathing crack. The signal is calculated at both ends of the beam to capture both the forward and backward scattered guided wave signals. The measurement duration covers the incident guided wave propagating to the beam end and reflecting back to the measurement location.

5.1. Incident S_0 guided wave

The first parametric study investigates the spectral amplitudes at the excitation frequency and each higher harmonic frequency as a function of crack depth when the incident wave is S_0 guided wave. Without loss of generality, the crack depth to beam height ratio (d_c/h) is used to present the results. A comparison of the Fourier-transformed in-plane velocity (S_0 guided wave) and mode-converted out-of-plane velocity (A_0 guided wave) is shown in Figure 19 for the backward crack-scattered guided wave and Figure 20 for the forward crack-scattered guided wave. It should be noted that the spectral amplitudes of the S_0 and mode-converted A_0 guided waves are normalised to the incident S_0 guided wave magnitude at f_0 =25 kHz.

Comparing Figure 19 with Figure 20, we can see that the FFTs of the backward and forward scattered guided wave signals from the crack are almost identical when using S_0 incident guided waves. Specifically, the spectral amplitudes at f_0 and $2f_0$ of the in-plane velocity, as shown in Figures 19(a) and 20(a), increase with the crack depth to beam height ratio d_c/h. We found that the spectral amplitude at f_0 increases sharply with d_c/h while that at $2f_0$ increases slowly and stably. We can see that the normalised spectral amplitude of the in-plane velocity at $2f_0$ is comparable to that at f_0 when d_c/h is less than 0.3. This indicates that the nonlinear in-plane response is very sensitive to small cracks when using S_0 incident guided waves.

The spectral amplitudes of the mode-converted out-of-plane A_0 guided waves are shown in Figures 19(b) and 20(b). We can see that the normalised spectral amplitude of the fundamental harmonic (f_0) increases significantly with d_c/h and reaches its maximum at around 1.2 at d_c/h = 0.87. Then it decreases to 0.9 at d_c/h = 0.99. The normalised spectral amplitude of the second harmonic (at $2f_0$) begins to increase slowly with d_c/h. It reaches the maximal value just below 0.3 when d_c/h = 0.65. Later, it starts to decrease stably with d_c/h and finally reaches 0.13. Overall, the amplitude of the second harmonic is small when compared with the linear signal in the mode-converted out-of-plane velocity.

[Figure 19. Fourier-transformed (a) in-plane and (b) mode-converted out-of-plane velocity as a function of crack depth to beam height ratio (d_c/h) at measurement location x = 0 m when the incident wave is S_0 guided wave]

[Figure 20. Fourier-transformed (a) in-plane and (b) mode-converted out-of-plane velocity as a function of crack depth to beam height ratio (d_c/h) at measurement location x = 1 m when the incident wave is S_0 guided wave]

Comparing Figures 19(a) and 20(a) with Figures 19(b) and 20(b), the results show that the normalised spectral amplitude of the second harmonic (at $2f_0$) of the mode-converted A_0 guided waves are generally larger than the S_0 guided waves when the crack is small (i.e., $d_c/h < 0.65$). As the crack continues to grow (i.e., $d_c/h > 0.75$), the normalised spectral amplitude of the second harmonic ($2f_0$) of the mode-converted A_0 becomes smaller than that of the S_0 guided wave signal. This indicates that the second harmonic of the mode-converted out-of-plane A_0 guided wave is more sensitive than the in-plane S_0 guided wave in detecting smaller cracks when the incident wave is the S_0 guided wave.

5.2. Incident A_0 guided wave

The second parametric study examines the A_0 guided wave excited in the aluminium beam. The Fourier-transformed out-of-plane (A_0 guided wave) and in-plane (S_0 guided wave) velocities are shown in Figures 21 and 22. The spectral amplitudes are

normalised to the maximal spectral amplitude of the A_0 incident wave at f_0 =25 kHz. Figure 21(a) shows the FFT out-of-plane velocity of the backward scattered guided wave induced by the crack. The normalised spectral amplitude of the fundamental harmonic (f_0) increases significantly from 0 to just below 0.4 at d_c/h = 0.65. Then it decreases sharply with the crack growth, to around 0.05 when d_c/h = *0.99*. This pattern is different to that using the S_0 incident guided wave in Figure 19(a) due to the difference of the mode-shape between S_0 and A_0 guided waves [65]. In contrast, the normalised spectral amplitude of the second harmonic ($2f_0$) increases slowly from 0 to 0.11 at d_c/h = *0.55*, while it decreases to 0.8 when d_c/h = *0.85*. After that, it increases suddenly to 0.35 at d_c/h = *0.99*.

[Figure 21. Fourier-transformed (a) out-of-plane and (b) mode-converted in-plane velocity as a function of crack depth to beam height ratio (d_c/h) at measurement location x = 0 m when the incident wave is A_0 guided wave]

On the other hand, Figure 22(a) illustrates the FFT out-of-plane velocity of the forward scattered A_0 guided wave induced by the crack. The normalised spectral amplitude of the fundamental harmonic (f_0) increases with d_c/h. When d_c/h < 0.65, it increases significantly from 0 to around 0.5. When 0.65 < d_c/h < 0.9, it slowly increases from 0.5 to 0.6. After d_c/h > 0.9, the amplitude increases dramatically to just below 1. In comparison, the spectral amplitude of the second harmonic of the forward scattered guided wave has a similar trend to the backward scattered guided wave as shown in Figure 21. The amplitude of the second harmonic forward scattered guided wave is larger than the backward scattered guided wave. As shown in Figure 22(a), the second harmonic has the first peak at d_c/h = 0.55 with a normalised amplitude around 0.18, then it reduces to 0.15 at d_c/h = 0.85. Finally, it increases to around 0.6 when d_c/h = 0.99.

[Figure 22. Fourier-transformed (a) out-of-plane and (b) mode-converted in-plane velocity as a function of crack depth to beam height ratio (d_c/h) at measurement location x = 1 m when the incident wave is A_0 guided wave]

Figures 21(b) and 22(b) show the normalised spectral amplitude of the mode-converted S_0 guided wave (in-plane velocity), which are almost identical. We can see that the normalised spectral amplitude of the mode-converted fundamental harmonic

increases with the crack growth, and peaks at d_c/h = 0.9 with the value 0.28. After that, it decreases to just above 0.2 at d_c/h = 0.99. The amplitude of the second harmonic increases slowly to around 0.08 at d_c/h = 0.65, then it decreases slightly to 0.07 at d_c/h = 0.9. After that, it increases again to 0.11 at d_c/h = 0.99.

Comparing Figure 21 with Figure 22, it is shown that the energy of the reflected out-of-plane linear guided wave decreases from d_c/h = 0.65, while that of the transmitted out-of-plane guided wave increases. This indicates that the energy of the reflected out-of-plane linear guided wave converts to that of the transmitted out-of-plane guided wave from d_c/h = 0.65. After d_c/h = 0.85, the energy of the reflected out-of-plane linear guided wave decreases dramatically. Also, the energy of both the mode-converted reflected and transmitted in-plane linear guided waves decrease from d_c/h = 0.85. However, the energy of the transmitted out-of-plane linear guided wave and the energy of all the in-plane and out-of-plane nonlinear guided waves increase significantly from d_c/h = 0.85. This demonstrates the energy conversion from the reflected out-of-plane linear guided wave and the mode-converted in-plane guided waves to transmitted out-of-plane linear guided wave and other nonlinear guided waves.

Comparing Figures 19 and 20 with Figures 21 and 22, we can see that when the incident wave is an S_0 guided wave, the spectral amplitudes of the second harmonics due to contact nonlinearity are larger than that of using the A_0 guided wave as the incident wave for small crack (e.g. d_c/h <0.3). When the crack becomes large (e.g. d_c/h >0.8), the second harmonics induced by contact nonlinearity when using an S_0 incident wave becomes smaller than when an A_0 incident wave is used. This indicates that the S_0 guided wave is more suitable as the incident wave for detecting small cracks when we consider contact nonlinearity and the mode-conversion effect. In contrast, A_0 guided waves are more suitable for larger cracks.

6. Conclusions

This study has proposed the modelling and investigated of the interaction of nonlinear guided waves at breathing cracks. An extended time-domain SFE method has been proposed to improve the efficiency of simulation. The method considers the coupling of longitudinal, transverse and rotation DoFs based on the Mindlin-Hermann rod and Timoshenko beam theories. An SFE crack element has been developed to simulate the mode-conversion effect of guided waves when they interact with an asymmetric crack.

A bilinear crack mechanism has been proposed to simulate the crack opening and closing. This has been embedded in the SFE crack element to simulate contact nonlinearity.

This paper has presented numerical verification to demonstrate the accuracy of the proposed SFE model in simulating the contact nonlinearity. Very good agreement has been found between the time-domain SFE and explicit 3D FE results, which shows the accuracy of the proposed SFE model. The characteristics of the higher harmonics generated by the contact nonlinearity and mode-conversion effect at the asymmetric crack have been studied in detail using the extended SFE model. This paper has also presented parametric studies to investigate the magnitude of the higher harmonics generation by S_0 and A_0 guided waves. The normalised spectral amplitude as a function of the crack depth to beam height ratio has been investigated. The paper has shown that with the consideration of the mode-conversion effect, the higher harmonic generation by the S_0 incident guided wave has a larger magnitude than that by the A_0 incident guided wave.

Overall the study has provided physical insights into the higher harmonic generation at the breathing crack by S_0 and A_0 guided waves. The simulation has been conducted using the proposed computationally efficient SFE model. This SFE model can be further applied in the fields of damage identification.

Acknowledgement

This work was supported by the Australian Research Council (ARC) under Grant Numbers DP160102233 and DE130100261. The support is greatly appreciated.

References

[1] Magalhães F, Cunha A and Caetano E 2012 *MSSP* **28** 212-228.
[2] Lam H and Yin T 2010 *Eng. Struct.* **32** (10) 3145-3152.
[3] Yin T, Lam H F, Chow H M and Zhu H 2009 *Eng. Struct.* **31** (9).
[4] Nair A and Cai C S 2010 *Eng. Struct.* **32** (6) 1704-1714.
[5] Achenbach J 2000 *IJSS* **37** (1) 13-27.
[6] Mitra M and Gopalakrishnan S 2016 *Smart Mater. Struct.* **25** (5) 053001.
[7] Ng C 2015 *Int. J. Struct. Stab. Dyn.* **15** (08) 1540010.
[8] Ng C-T 2015.
[9] He J and Yuan F-G 2016 *Smart Mater. Struct.* **25** (10) 105022.
[10] Gangadharan R, Bhat M, Murthy C and Gopalakrishnan S 2010 *Smart Mater. Struct.* **19** (11) 115010.

[11] Kim S B and Sohn H 2007 *Smart Mater. Struct.* **16** (6) 2375.
[12] Ng C T 2014 *Struct. Health Monit.* **13** (4) 359-373.
[13] Kažys R, Raišutis R, Žukauskas E, Mažeika L and Vladišauskas A 2010 *Physics Procedia* **3** (1) 185-192.
[14] Pau A and Vestroni F 2011 *J. Intell. Mater. Syst. Struct.* **22** (16) 1869-1877.
[15] Quek S T, Tua P and Wang Q 2003 *Smart Mater. Struct.* **12** (3) 447.
[16] Flynn E B, Todd M D, Wilcox P D, Drinkwater B W and Croxford A J 2011 presented at the Proceedings of the Royal Society of London A: Mathematical, Physical and Engineering Sciences.
[17] Ng C, Veidt M and Rajic N 2009 presented at the Second International Conference on Smart Materials and Nanotechnology in Engineering.
[18] Aryan P, Kotousov A, Ng C and Cazzolato B 2016 *Struct. Contr. Health Monit.*
[19] Tian Z, Yu L, Leckey C and Seebo J 2015 *Smart Mater. Struct.* **24** (10) 105019.
[20] Zhao X, Gao H, Zhang G, Ayhan B, Yan F, Kwan C and Rose J L 2007 *Smart Mater. Struct.* **16** 1208-1217.
[21] Sohn H, Dutta D, Yang J, DeSimio M, Olson S and Swenson E 2011 *Smart Mater. Struct.* **20** (4) 045017.
[22] Han J-H and Kim Y-J 2015 *MSSP* **54** 336-356.
[23] He S and Ng C-T 2016 *Eng. Struct.* **127** 602-614.
[24] Sohn H, Park H W, Law K H and Farrar C R 2007 *J. Aerospace Eng.* **20** (3) 141-151.
[25] Kawashima K, Omote R, Ito T, Fujita H and Shima T 2002 *Ultrasonics* **40** (1–8) 611-615.
[26] Solodov I Y, Krohn N and Busse G 2002 *Ultrasonics* **40** (1) 621-625.
[27] Pieczonka L, Klepka A, Martowicz A and Staszewski W J 2016 *OptEn* **55** (1) 011005-011005.
[28] Dziedziech K, Pieczonka L, Kijanka P and Staszewski W J 2016 *Struct. Contr. Health Monit.*
[29] Yan D, Neild S A and Drinkwater B W 2012 *NDT & E International* **47** 18-25.
[30] Najib M F and Nobari A S 2015 *Int. J. Adhes. Adhes.* **63** 46-56.
[31] Soleimanpour R, Ng C T and Wang C H 2016 *Struct. Health Monit.* 1475921716673021.
[32] Soleimanpour R and Ng C-T 2016 *Eng. Struct.*
[33] Broda D, Staszewski W J, Martowicz A, Uhl T and Silberschmidt V V 2014 *J. Sound Vibrat.* **333** (4) 1097-1118.
[34] Willberg C, Duczek S, Vivar-Perez J and Ahmad Z 2015 *ApMRv* **67** (1) 010803.
[35] Aryan P, Kotousov A, Ng C and Wildy S 2016 *Smart Materials and Structures* **25** (3) 035018.
[36] Zhou W J and Ichchou M N 2011 *Struct. Health Monit.* **10** (4) 335-349.
[37] Nag A, Mahapatra D R and Gopalakrishnan S 2002 *Smart Materials and Structures* **11** (6) 899.
[38] Park I, Kim S and Lee U 2013 *Smart Materials and Structures* **22** (7) 075034.
[39] Mahapatra D R, Singhal A and Gopalakrishnan S 2006 *Computer methods in applied mechanics and engineering* **195** (9) 1116-1135.
[40] Joglekar D and Mitra M 2016 *MSSP* **76** 576-591.
[41] Samaratunga D, Jha R and Gopalakrishnan S 2014 *Compos. Struct.* **108** 341-353.
[42] Gopalakrishnan S and Mitra M, *Wavelet methods for dynamical problems: with application to metallic, composite, and nano-composite structures*. (CRC Press, 2010).
[43] Zhao X G and Rose J L 2003 *IJSS* **40** (11) 2645-2658.

[44] Xu F, Zhang Y, Hong W, Wu K and Cui T J 2003 *Microwave Theory and Techniques, IEEE Transactions on* **51** (11) 2221-2227.
[45] Hayashi T and Kawashima K 2002 *Ultrasonics* **40** (1) 193-197.
[46] Wang X, Wang F, Xu C and Ge L 2012 *Nanjing Hangkong Hangtian Daxue Xuebao/Journal of Nanjing University of Aeronautics and Astronautics* **44** (5) 645-651.
[47] Rucka M, Witkowski W, Chróścielewski J and Wilde K 2012 *Archives of Civil Engineering* **58** (1) 3-24.
[48] Li F, Peng H, Sun X, Wang J and Meng G 2012 *Mathematical Problems in Engineering* **2012**.
[49] Ostachowicz W M 2008 *Computers & structures* **86** (3) 454-462.
[50] Żak A, Radzieński M, Krawczuk M and Ostachowicz W 2012 *Smart Materials and Structures* **21** (3) 035024.
[51] Kudela P, Krawczuk M and Ostachowicz W 2007 *Journal of sound and vibration* **300** (1) 88-100.
[52] Kudela P and Ostachowicz W 2009 *Mechanics of Advanced Materials and Structures* **16** (3) 174-187.
[53] Giannini O, Casini P and Vestroni F 2013 *Computers & Structures*.
[54] Xu F, Wu K and Hong W 2007 *IEEE Transactions on Microwave Theory and Techniques* **55** (4) 697-702.
[55] Shen Y and Cesnik C E 2016 *Ultrasonics*.
[56] Joglekar D and Mitra M 2015 *Smart Mater. Struct.* **24** (11) 115004.
[57] He S and Ng C-T 2017 *MSSP* **84** 324-345.
[58] Rucka M 2010 *Archive of Applied Mechanics* **80** (12) 1371-1390.
[59] He S and Ng C 2015 *Elec J Struct Eng* **14** 20-32.
[60] Darpe A, Gupta K and Chawla A 2004 *J. Sound Vibrat.* **269** (1) 33-60.
[61] Tada H, Paris P C, Irwin G R and Tada H, *The stress analysis of cracks handbook*. (ASME press New York, 2000).
[62] Bovsunovsky A and Surace C 2015 *MSSP* **62** 129-148.
[63] Aryan P, Kotousov A, Ng C T and Cazzolato B 2016 *Struct. Contr. Health Monit.*
[64] Ng C-T 2014 *Engineering Structures* **67** 50-60.
[65] Lowe M J, Cawley P, Kao J and Diligent O 2002 *The Journal of the Acoustical Society of America* **112** (6) 2612-2622.

Tables

Table 1. Summary of the time-domain SFE models used in the validation

Incident guided wave	S_0	A_0
Beam length L (m)	1	
Crack location L_c (m)	0.5	
Crack depth d_c (m)	0.003	
Young's modulus (GPa)	70	
Density (kg/m^3)	2700	
Poisson's ratio	0.3	

Table 2. Summary of case studies for higher harmonic generation due to contact nonlinearity at crack

Incident guided wave	S_0				A_0			
Damage cases	S1	S2	S3	S4	A1	A2	A3	A4
Beam length L (m)	6				3			
Crack location L_c (m)	1.9				0.95			
Crack depth d_c (m)	0.003							
Measured location (m)	x = 5				x = 1.65			
Contact nonlinearity effect	No	Yes	Yes	No	No	Yes	Yes	No
Mode conversion effect	No	No	Yes	Yes	No	No	Yes	Yes

Figures

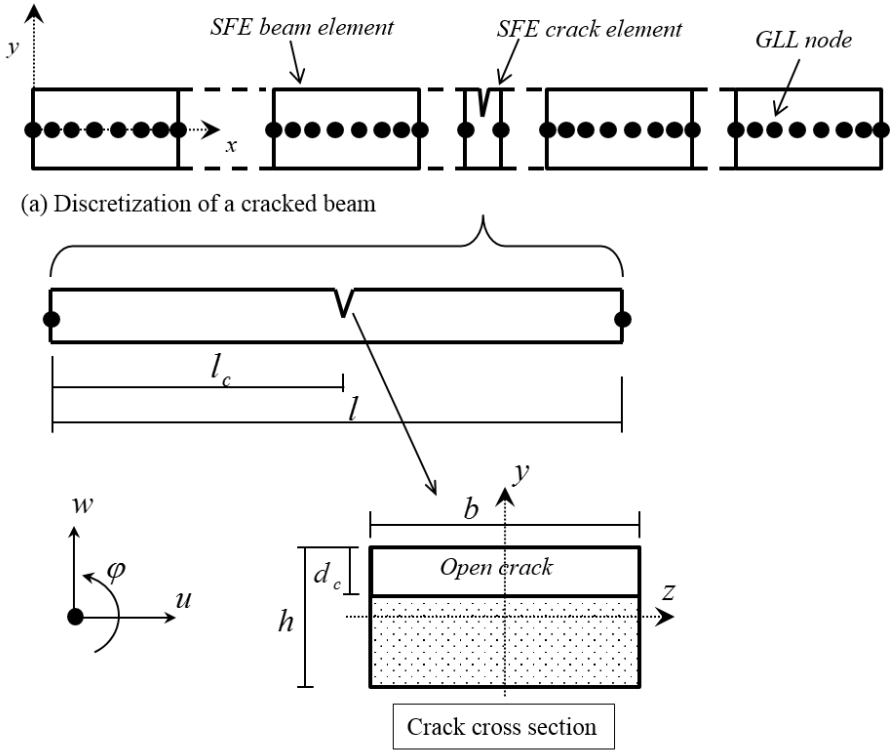

[Figure 1. Schematic diagram of the two-node crack element for simulating an opened crack. (a) Discretization of a cracked beam; (b) SFE crack element]

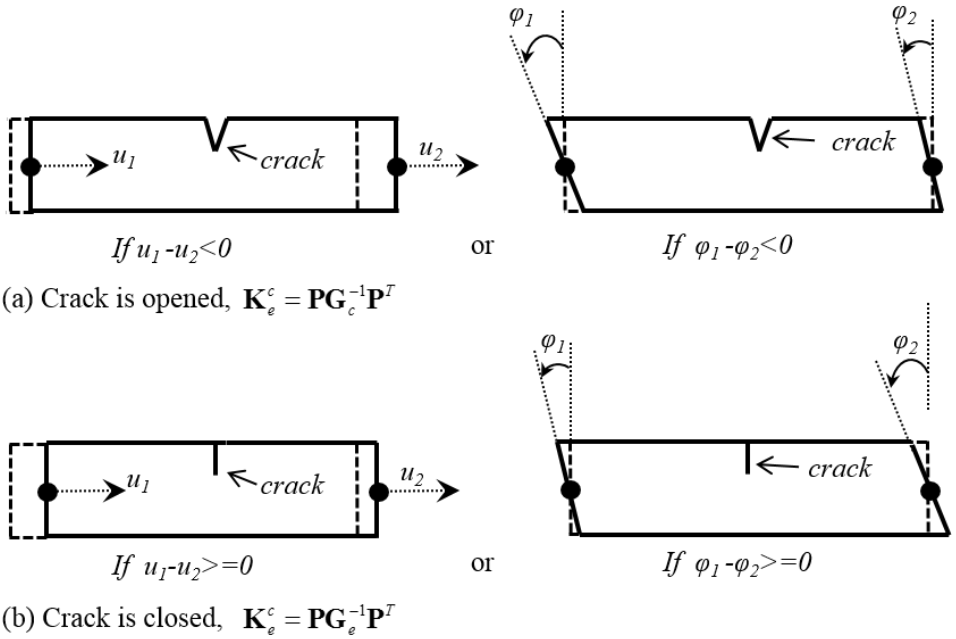

[Figure 2. Degrees-of-freedom at the crack element when the crack is (a) open and (b) closed]

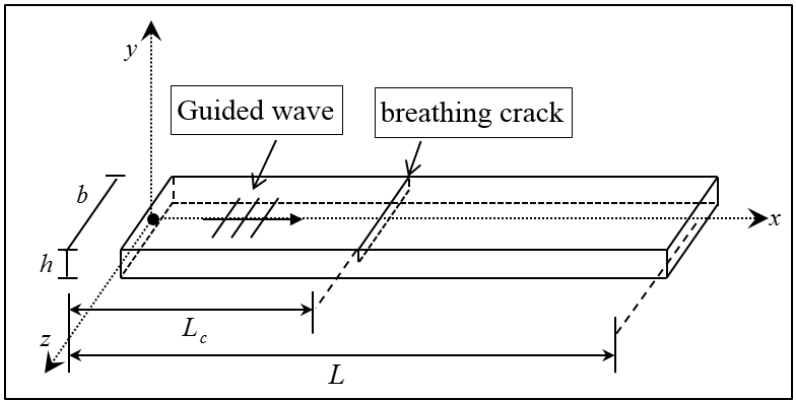

[Figure 3. Schematic diagram of a beam with a surface breathing crack]

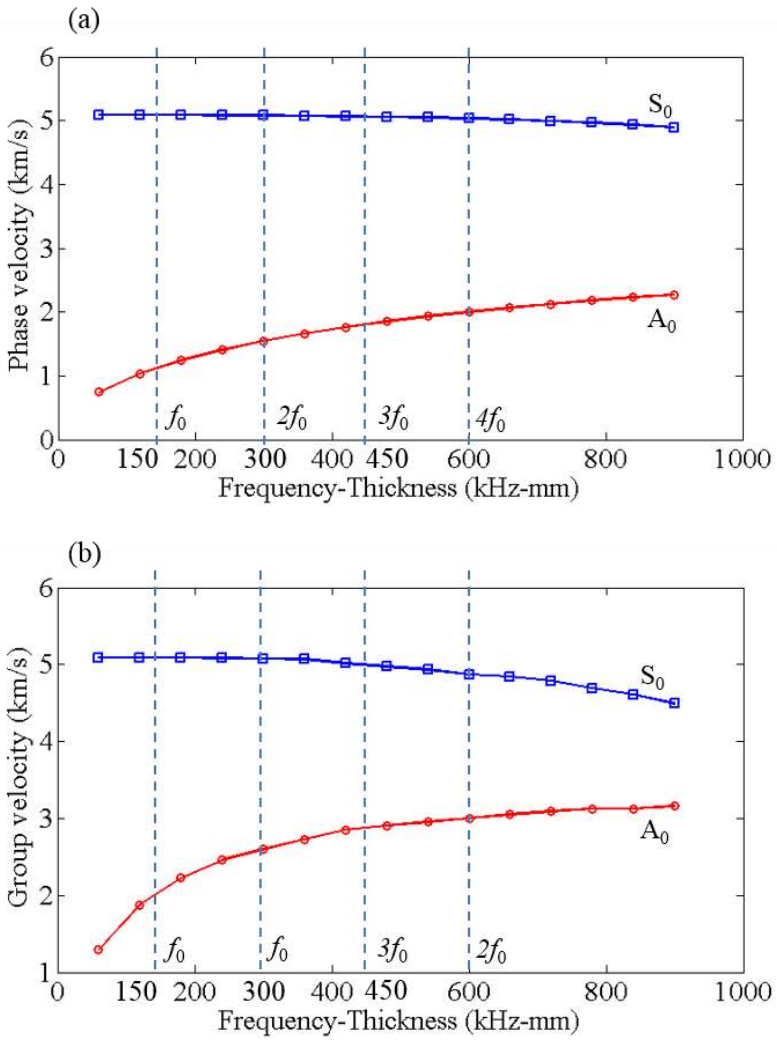

[Figure 4. Dispersion relations for an aluminum beam predicted by the SFE model (a) Phase velocity; (b) Group velocity]

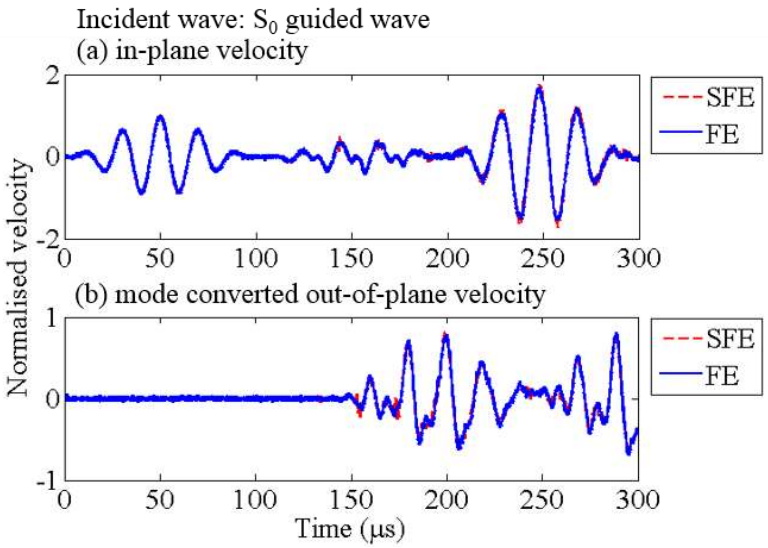

[Figure 5. Time-domain (a) in-plane and (b) mode converted out-of-plane velocity at x = 0 m for incident S_0 guided wave]

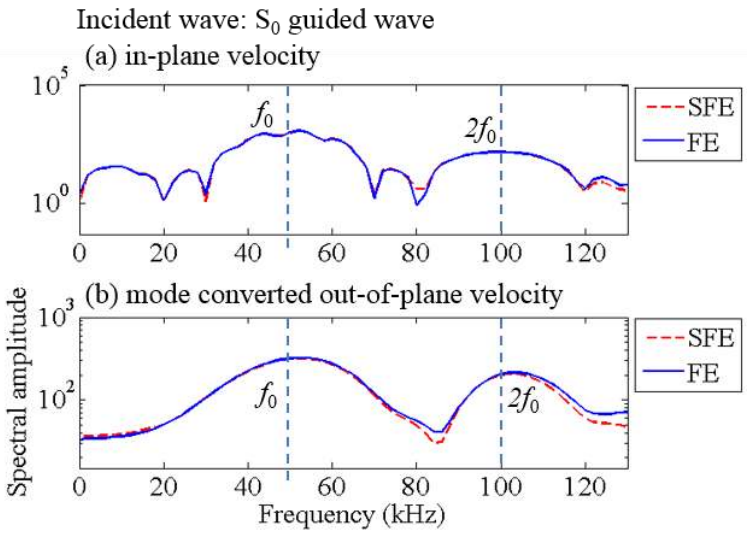

[Figure 6. Fourier transformed (a) in-plane and (b) mode converted out-of-plane velocity at x = 0 m for incident S_0 guided wave]

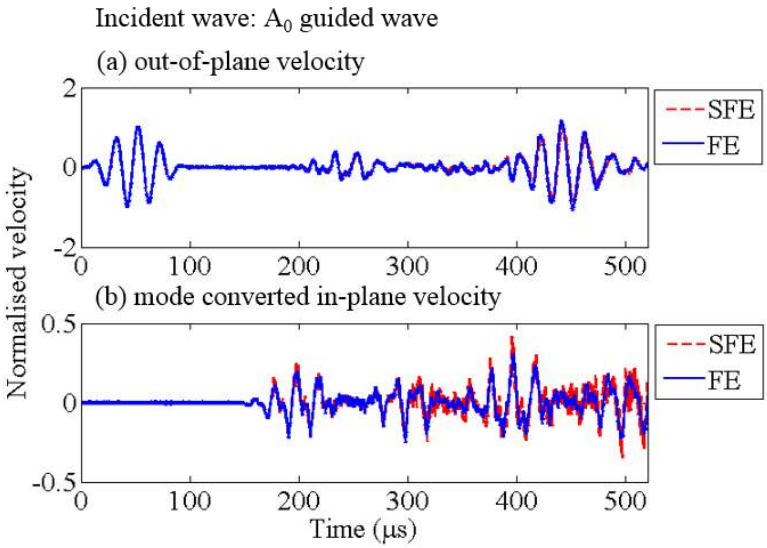

[Figure 7. Time-domain (a) out-of-plane and (b) mode converted in-plane velocity at x = 0 m for incident A_0 guided wave]

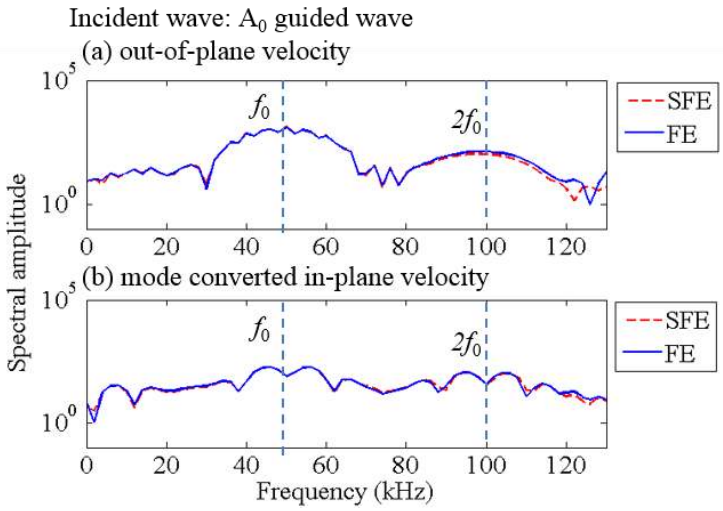

[Figure 8. Fourier transformed (a) out-of-plane and (b) mode converted in-plane velocity at x = 0 m for incident A_0 guided wave]

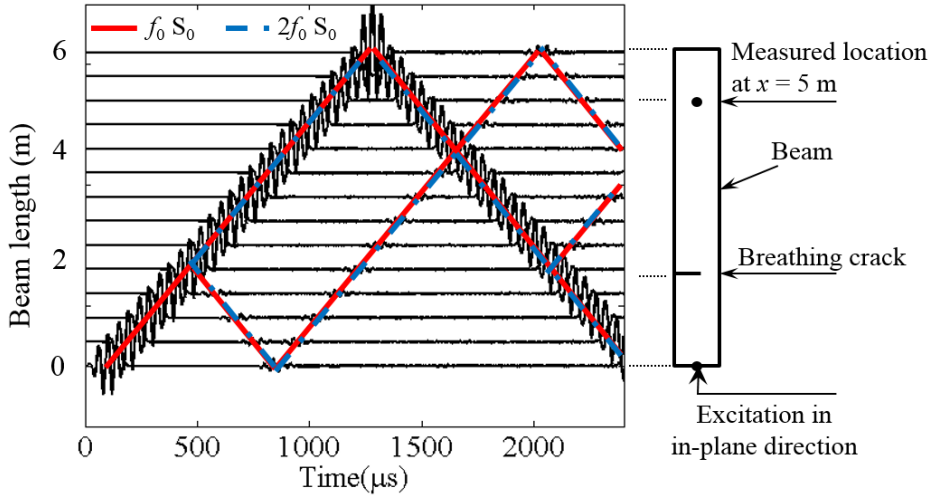

[Figure 9. In-plane velocity of S_0 guided wave time histories at different locations along the beam for Case S3]

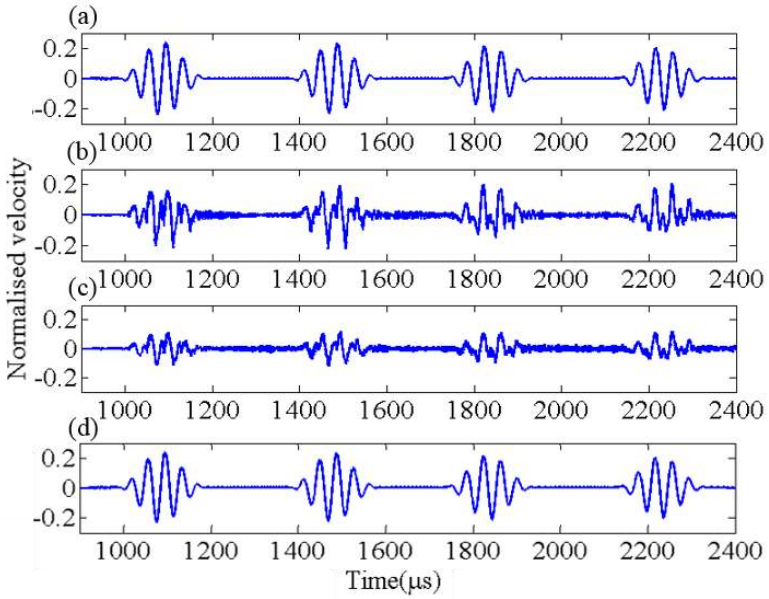

[Figure 10. Extracted time domain in-plane velocity signal from 900 - 2400 μs at x = 5 m for (a) Cases S1, (b) S2, (c) S3 and (d) S4]

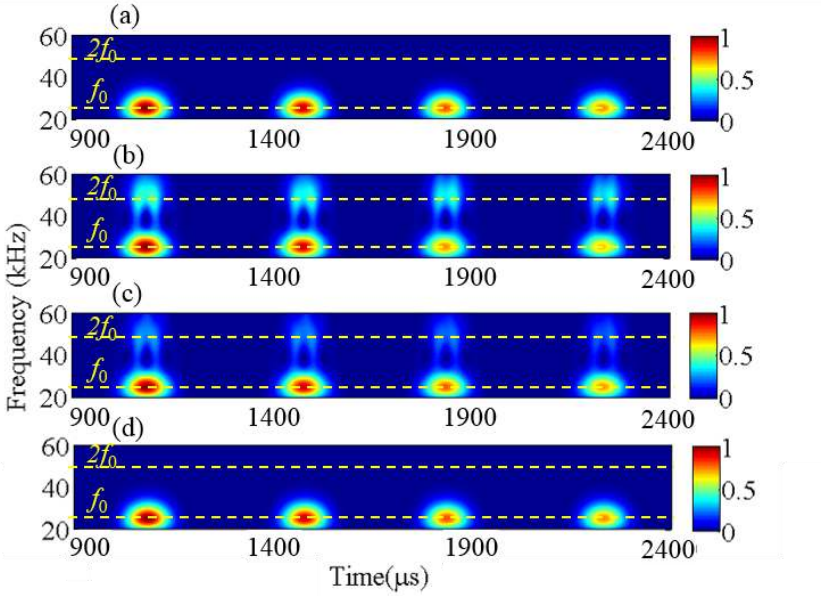

[Figure 11. Energy density spectrum of the in-plane velocity signal from 900 - 2400 μs at measurement location x = 5 m for (a) Cases S1, (b) S2, (c) S3 and (d) S4]

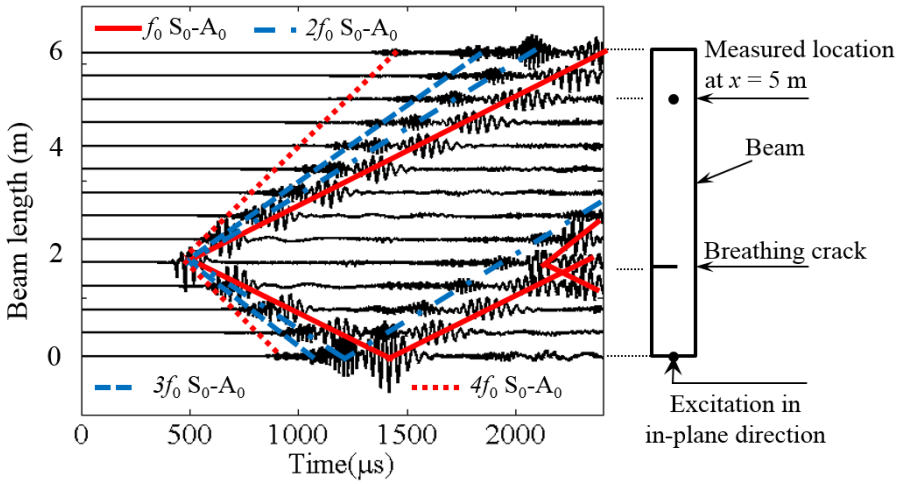

[Figure 12. Out-of-plane velocity of mode converted S_0-A_0 guided wave time history at different locations along the beam for Case S3 (the normalized amplitude is amplified by a factor of 3)]

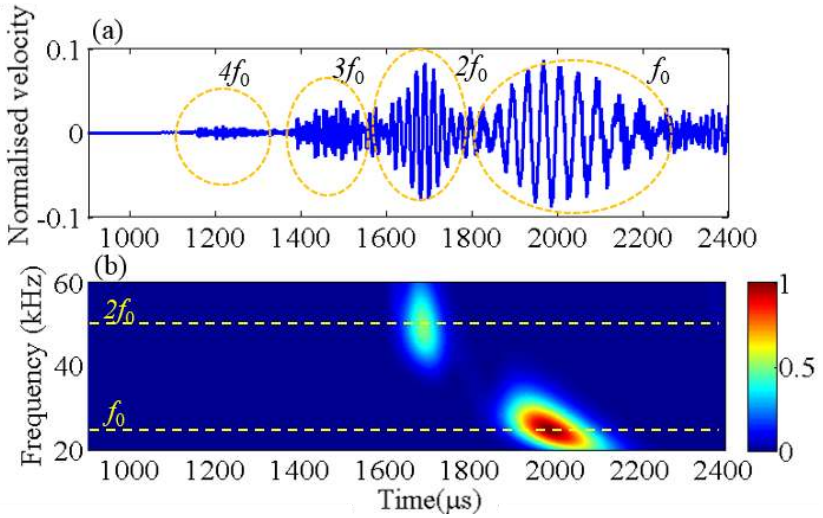

[Figure 13. Time history and energy density spectrum of the out-of-plane velocity signal from 900 - 2400 μs at measurement location x = 5 m for Cases S3]

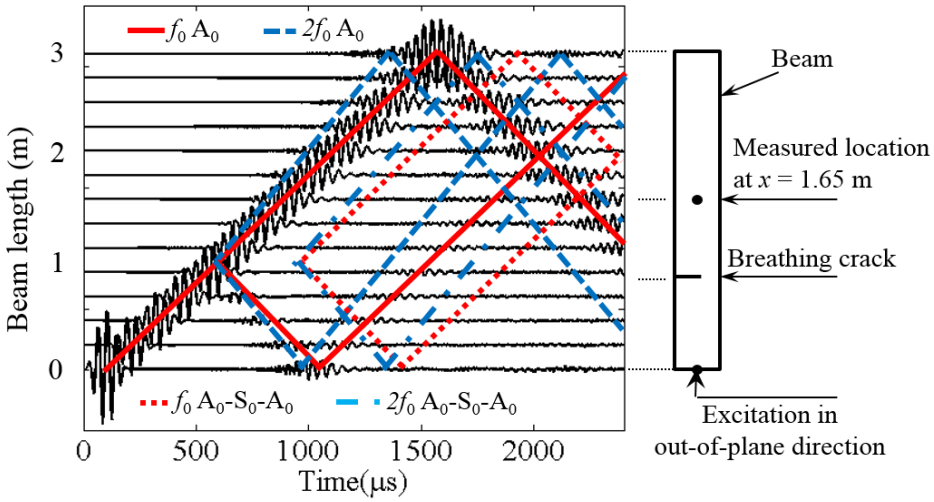

[Figure 14. Out-of-plane velocity of A_0 guided wave and mode converted A_0-S_0-A_0 guided wave time histories at different locations along the beam for Case A3]

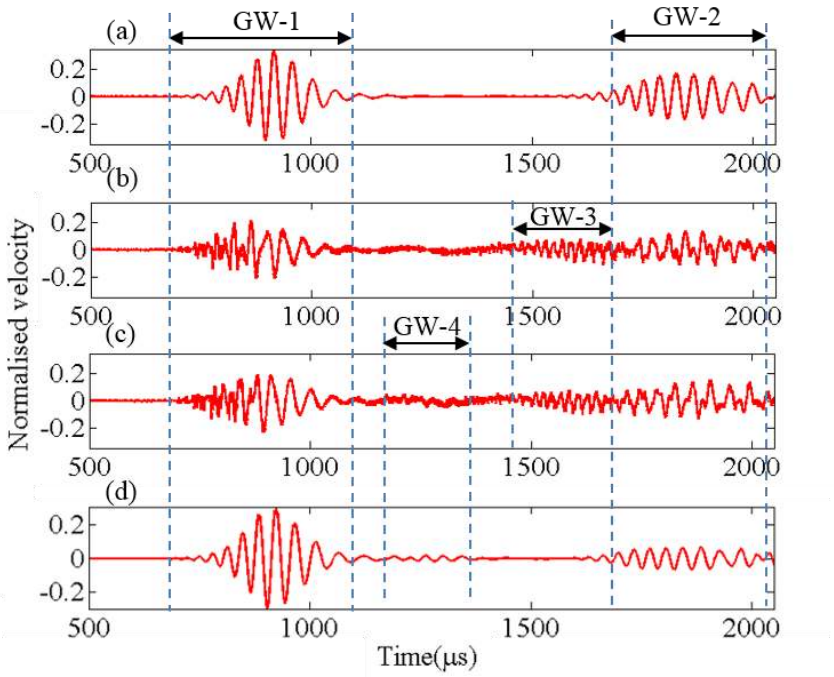

[Figure 15. Extracted time-domain out-of-plane velocity signal from 500 - 2100 μs at x = 1.65 m for (a) Cases A1, (b) A2, (c) A3 and (d) A4]

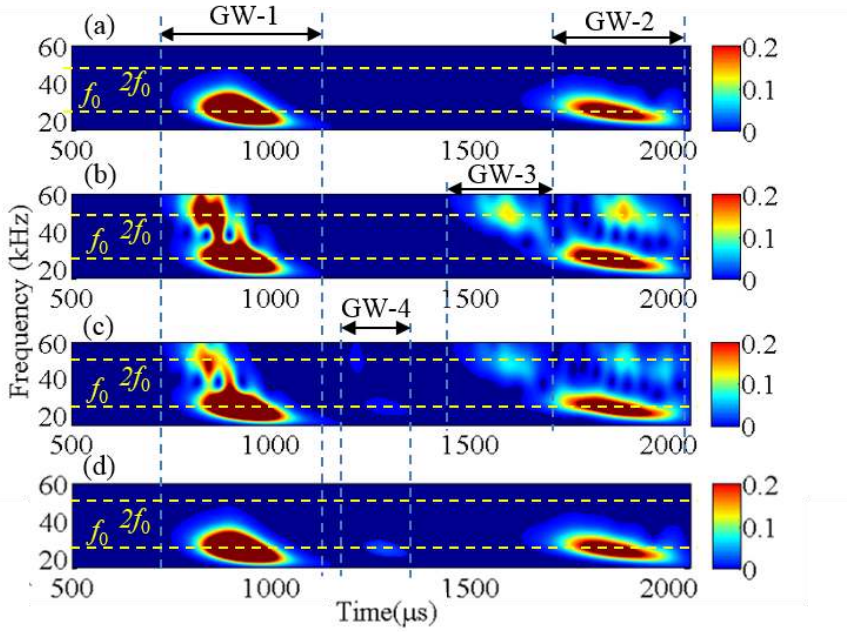

[Figure 16. Energy density spectrum of the out-of-plane velocity signal from 500 - 2100 μs at measurement location x = 1.65 m for (a) Cases A1, (b) A2, (c) A3 and (d) A4]

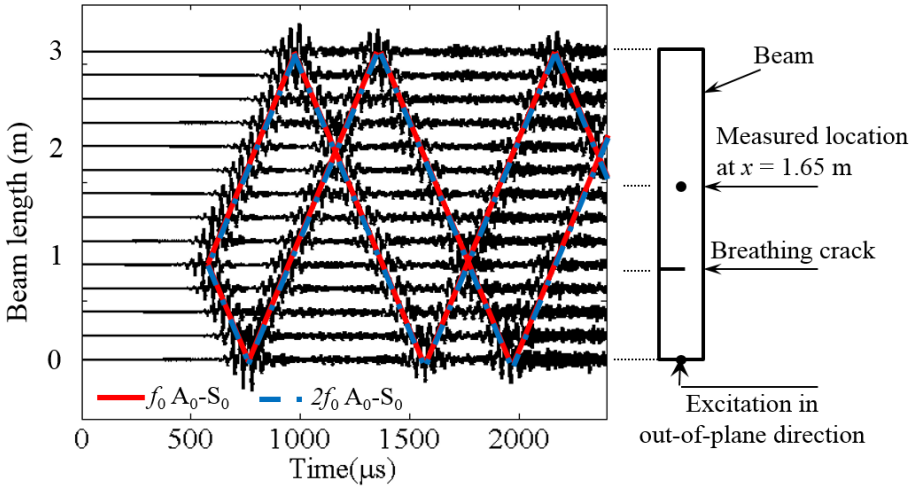

[Figure 17. In-plane velocity of mode converted A_0-S_0 *guided wave time histories at different locations along the beam for Case A3 (the normalised amplitude is amplified by a factor of 5)]*

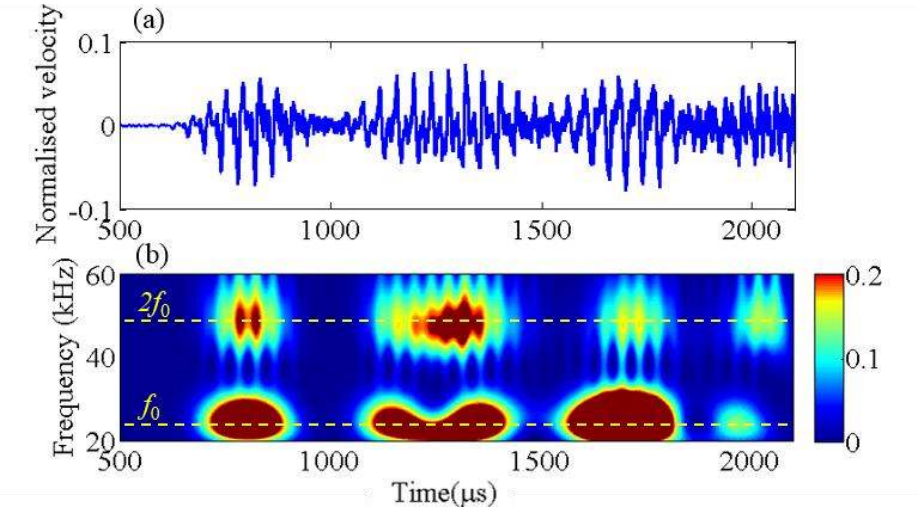

[Figure 18. Energy density spectrum of the in-plane velocity signal from 500 - 2100 μs at measurement location x = 1.65 m for Cases A3]

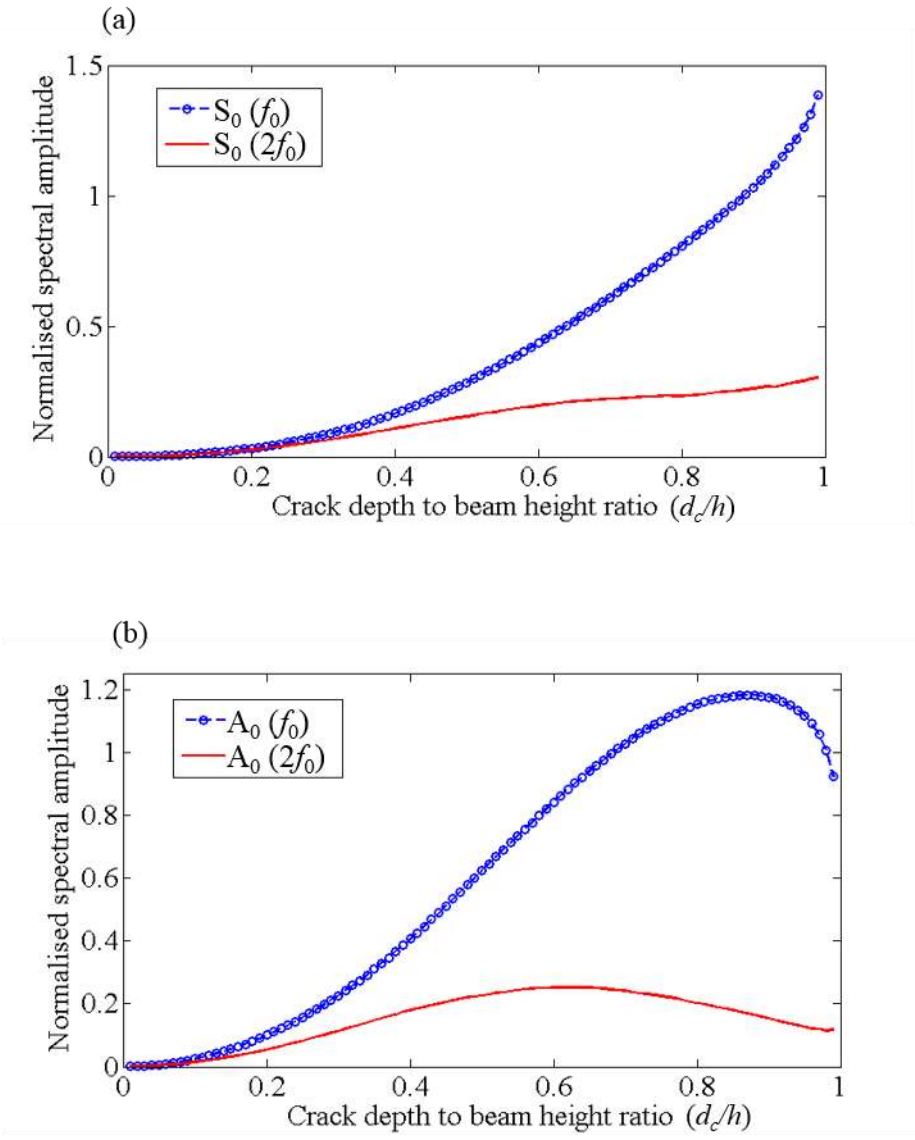

[Figure 19. Fourier transformed (a) in-plane and (b) mode converted out-of-plane velocity as a function of crack depth to beam height ratio (d_c/h) at measurement location x = 0 m when the incident wave is S_0 guided wave]

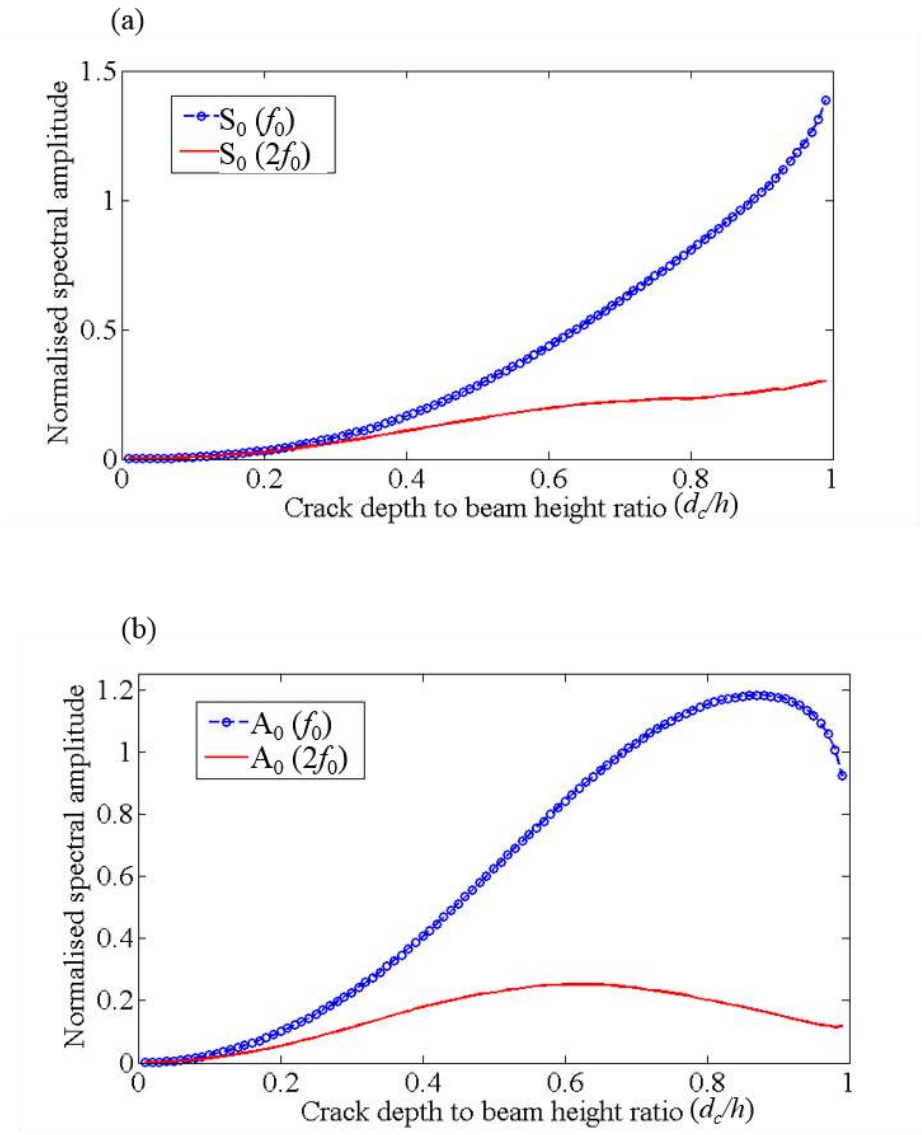

[Figure 20. Fourier transformed (a) in-plane and (b) mode converted out-of-plane velocity as a function of crack depth to beam height ratio (d_c/h) at measurement location x = 1 m when the incident wave is S_0 guided wave]

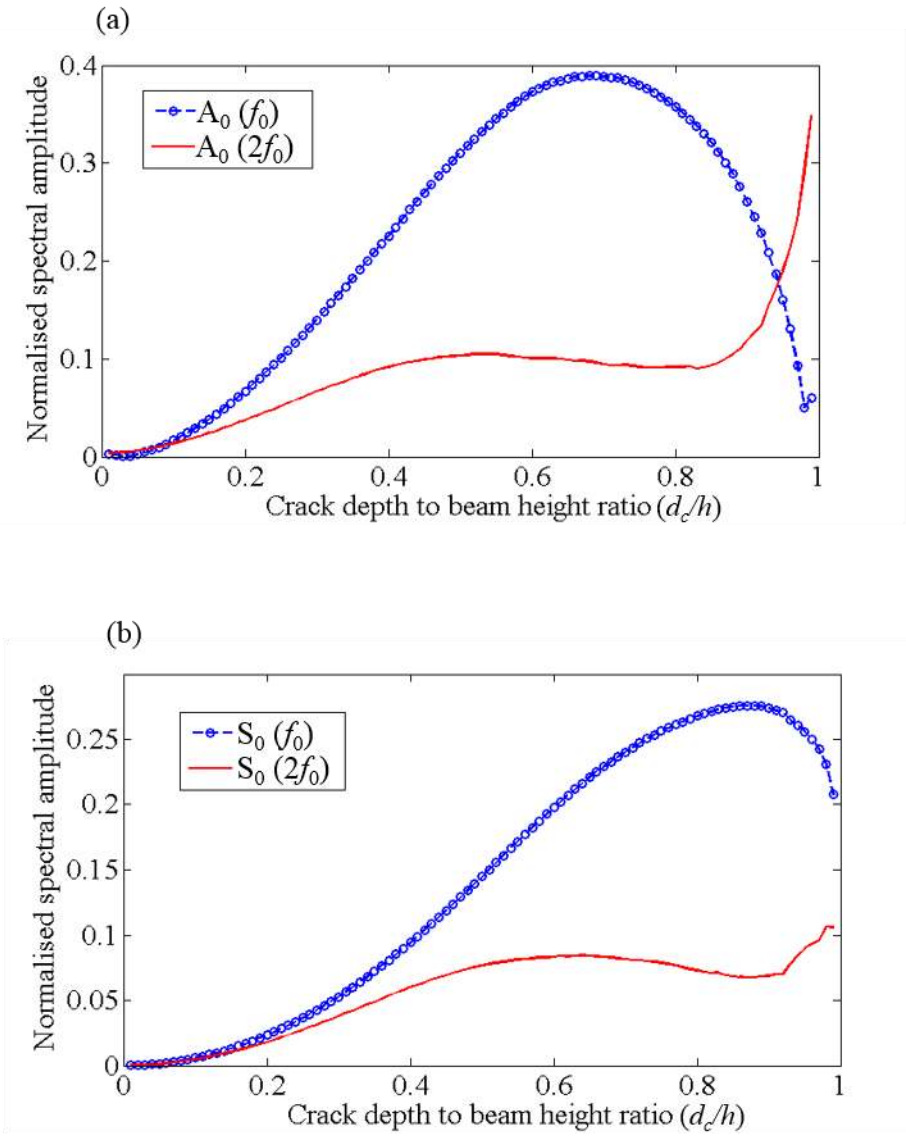

[Figure 21. Fourier transformed (a) out-of-plane and (b) mode converted in-plane velocity as a function of crack depth to beam height ratio (d_c/h) at measurement location x = 0 m when the incident wave is A_0 guided wave]

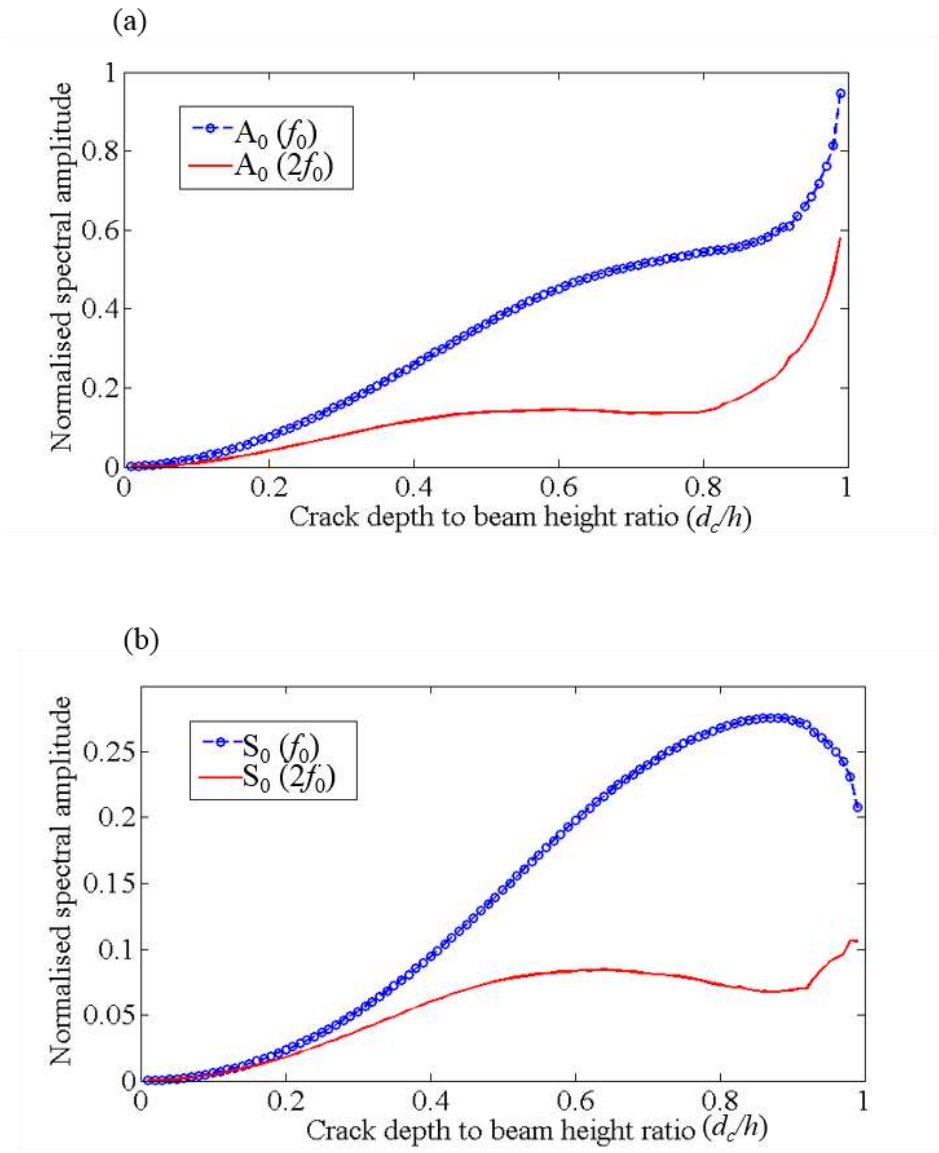

[Figure 22. Fourier transformed (a) out-of-plane and (b) mode converted in-plane velocity as a function of crack depth to beam height ratio (d_c/h) at measurement location x = 1 m when the incident wave is A_0 guided wave]